Measuring geometric imperfections of variable–angle filament–wound cylinders with a simple digital image correlation setup

Castro, Saullo G.P.; Almeida Jr., J.H.S.; St-Pierre, Luc; Wang, Z.

Important note
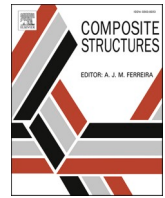To cite this publication, please use the final published version (if applicable).
Please check the document version above.

Measuring geometric imperfections of variable–angle filament–wound cylinders with a simple digital image correlation setup

Saullo G.P. Castro [a,*], José Humberto S. Almeida Jr. [b,c,*], Luc St-Pierre [b], Zhihua Wang [a,d]

[a] *Faculty of Aerospace Engineering, Delft University of Technology, Delft, The Netherlands*
[b] *Department of Mechanical Engineering, Aalto University, Espoo, Finland*
[c] *Advanced Composites Research Group, School of Mechanical and Aerospace Engineering, Queen's University Belfast, UK*
[d] *School of Mechanical and Electrical Engineering, University of Electronic Science and Technology of China, Chengdu, China*

ABSTRACT

Measuring the geometric imperfections in cylindrical shells is a critical step necessary to create accurate numerical models that can capture the imperfection-sensitive behavior of these structures. Modern composite structures, such as variable–angle filament–wound (VAFW) cylinders, have a unique imperfection signature that is still unknown to the scientific community. This new class of variable–stiffness structures developed by our research group combines wide tailoring capabilities with the efficient manufacturability enabled by filament winding process. The present study proposes a novel imperfection measurement method that is simple and applicable to both small and large structures. The topographic data is measured with only a pair of cameras. Practical aspects of using digital image correlation (DIC) are described and discussed in detail, such as lighting, focus adjustment, and calibration. State–of–the–art best–fit routines, based on least–squares optimization, are used to transform raw data into a common coordinate system. Finally, the transformed data is stitched to build a full 3D imperfection pattern that can be readily used in a nonlinear finite element analysis. The developed method is used to measure the imperfections of 12 VAFW cylinders. The mass of the cylinders is used to validate the geometric imperfections and evaluate the variability of the proposed methodology.

1. Introduction

The buckling performance of thin-walled structures can be significantly affected by uncertainties coming from load definitions, material properties, geometric variables and boundary conditions [1]. Fiber-reinforced composite materials are often employed in primary aeronautical and aerospace components because of their outstanding specific strength and stiffness, corrosion resistance, and high tailorability that allows design solutions not achievable with metals [2]. Aerospace structures usually consist of thin-walled shells that can buckle when subject to compressive loads. Curved shells, especially cylinders, can build a high membrane stress level under compression before buckling, becoming peculiarly sensitive to geometric imperfections [3]. This phenomenon was first observed by Southwell [4] in 1914, when isotropic cylindrical shells were found to buckle at considerably lower loads than theoretically predicted for geometrically-perfect cylinders. The first buckling design criteria for imperfect structures were proposed by Flügge [5] and Donnell [6], but these guidelines were mainly based

on empiricism. The classical reports from von Kármán and Tsien [7] and Koiter [8] confirmed the assumption that initial geometric imperfections, as deviations from an idealized geometry, are the primary source of discrepancy between predictions and experiments. These empirical factors, created to penalize the geometry and then referred to as knockdown factors (KDF), were applied with the objective of reducing the conservative predictions for the load carrying capacity. Although recognizably conservative, this method is still largely applied in preliminary design, such as with the NASA SP-8007 guideline [9].

The first work on imperfect fiber-reinforced composite shells was reported by Sheinman and Simitses [10]; their analytical model included axisymmetric-type geometric imperfections. They concluded that the imperfection sensitivity of orthotropic shells in axial compression decreases with both increasing radius-to-thickness (r/t ratio) and length-to-thickness (l/t ratio) values. Their assumptions were later confirmed [11] with axial compression tests on boron/epoxy composite cylinders [12]. Nevertheless, these assumptions were still considered as semi-empiric. The first direct measurement of geometric imperfections
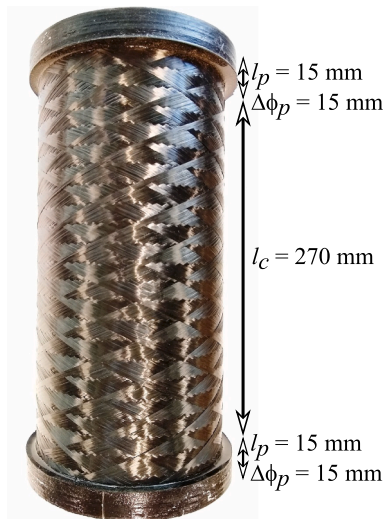
Fig. 1. Resin potting details, where l_c is the cylinder length, l_p is the resin potting length, and $\Delta\phi_p$ is the potting diameter variation.

Fig. 2. Filament-wound cylinders used in the imperfection measurements.

Fig. 3. Speckled patterns applied to each sample. Sparse and dense speckled patterns are preferred, avoiding large black areas to prevent loss of measured imperfection data.

Fig. 4. Experimental setup for the DIC measurements.

Fig. 5. Delft Aerospace Structures and Materials Laboratory (DASML) ambient lighting. The varying light affects the measurements, requiring on-the-fly adjustments of artificial light and camera exposure time.

was reported by Chryssanthopoulos et al. [13] for aramid/epoxy composite cylinders. They employed a linear voltage displacement transducer (LVDT) to measure inner and outer surfaces, in which the imperfections were recorded in an interval of 10 mm axially and 20 mm circumferentially. The external surface of the cylinder was adjusted using the so called "best-fit" procedure originally proposed by Arbocz and Babcock [14]. Thenceforth, the number of reports and methods increased substantially and it is well established that considering imperfections is vital to accurately predict the actual load carrying ability of shells [15].

Numerous approaches have been developed to include imperfections in numerical simulations. One of the most disseminated method is the linear buckling mode-shape imperfections (LBMI), initially proposed by Khot and Venkayya [16]. This approach uses axisymmetric mode-shapes, obtained through a linear buckling analysis, as geometric imperfections in a nonlinear analysis [17]. An advantage of the LBMI method is that the imperfection pattern is obtained from a computationally inexpensive eigenvalue buckling analysis, and it is straightforward to include such imperfections as an initial state to create a load path to reach the post-buckling state [18]. Another recent, but perhaps
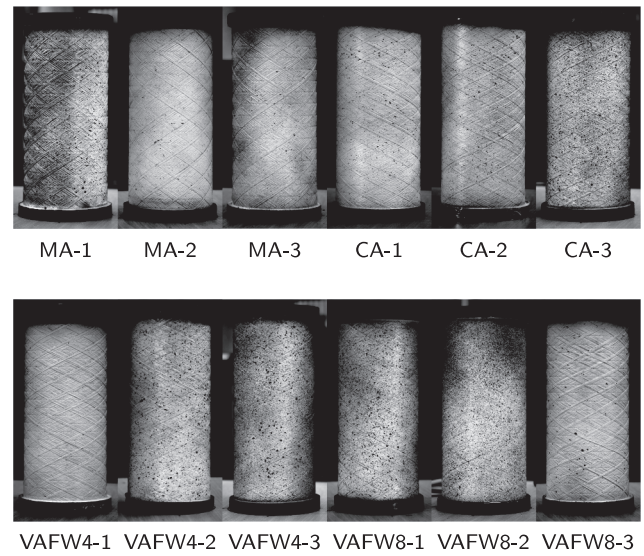
Fig. 6. Adjusted focus with a compromise between accuracy and surface depth coverage.

Too dark Dark Good Bright Too bright
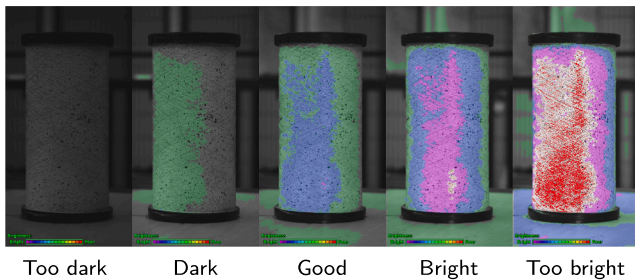
Fig. 7. DIC brightness conditions. Dark conditions are found if the exposure time is too small and there is no sufficient environmental light. Focused light produces undesirable reflections on the cylindrical surface.

equally well–disseminated approach, is the "single perturbation load approach (SPLA)", originally proposed by Hühne et al. [19]. This technique uses a small lateral load, prior or in addition to the axial compression, to trigger buckling. However, the SPLA does not consider other types of imperfections, e.g. load asymmetries [20]. Although LBMI, SPLA, and axisymmetric imperfections approaches can be realistic for shells with well-known or smooth surfaces, they can provide, nevertheless, inaccurate predictions for structures with complex architectures, such as modern cylinders with variable–angle tow (VAT) and/ or variable–thickness character [21] produced via advanced manufacturing techniques, such as filament winding. In these cases, it would be more appropriate to measure the imperfections after manufacturing, and this would require capturing mid–surface imperfections (MSI) and variations in thickness [22].

Degenhardt et al. [23] carried out an in-depth imperfections measurement of carbon fiber–reinforced polymer (CFRP) unstiffened cylinders. Firstly, they used automatic ultrasonic testing with water split

coupling to detect any defects in the structures. This method can also be employed to take full field thickness measurements. Secondly, they used an optical 3D digitizing system based on photogrammetry to extract, using the best–fit method, the actual radius of the cylinders and their initial geometric imperfections. To achieve this, they used four high-–speed cameras simultaneously to scan the whole cylinder, each covering 90° of the shell. Although precise, this measurement system is very expensive and complex to put in place. A similar system was successfully employed by Khakimova et al. [24] to measure thickness imperfections in unstiffened CFRP cylinders, also using the best–fit method. Otherwise, Eberlein [25] measured the imperfection signature of CFRP cylinders using a light scanner, a system also used by NASA. The measurements led to propose a KDF of 0.91, significantly less conservative than the value of 0.59 recommended in NASA SP-8007 guideline. Another approach is to use a laser scanner, as proposed by Skukis et al. [26]. The best-fit-cylinder algorithm was used to eliminate rigid body motion modes from the measurements. Their method, however, was not able to cover 360° of the cylinder and an error of 15% between experiments and predictions was found. Labans and Bisagni [27] measured the imperfections of VAT cylinders using a hybrid system, in which the outer surface was scanned using digital image correlation (DIC), and the inner surface with a laser distance sensor. As a key achievement, they found that VAT cylinders are less sensitive to geometric imperfections than constant–stiffness shells. Finally, a few conclusions can be drawn from these studies:

- the setups necessary to measure imperfections are very expensive and complex;
- there is no well established procedure to capture 360° of a 3D structure; and
- there is no work detailing the complete step-by-step procedure to measure the mid-surface imperfection of a 3D structure via DIC.

In addition to these identified issues, it is well–established that filament winding (FW) [28] is the most suitable and fastest
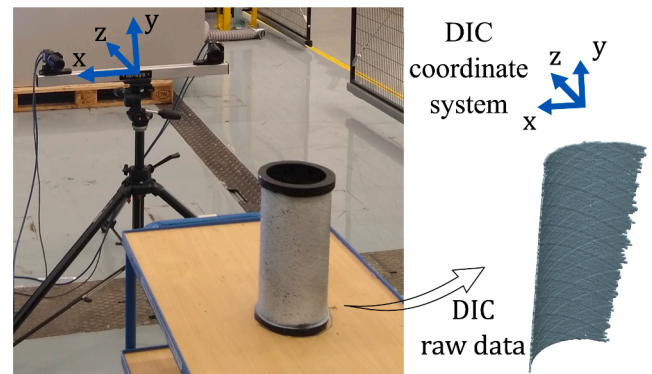

Fig. 9. DIC coordinate system and example of raw data. The raw data consists of a topological representation of the cylinder outer surface, discretized by points.
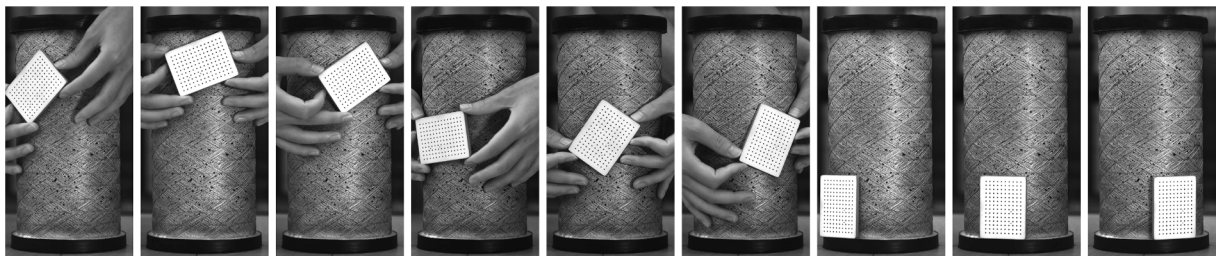

Fig. 8. DIC calibration images for sample MA1-1. The calibration pattern of 5 mm is placed at nine positions defining the extremities of the region of interest.
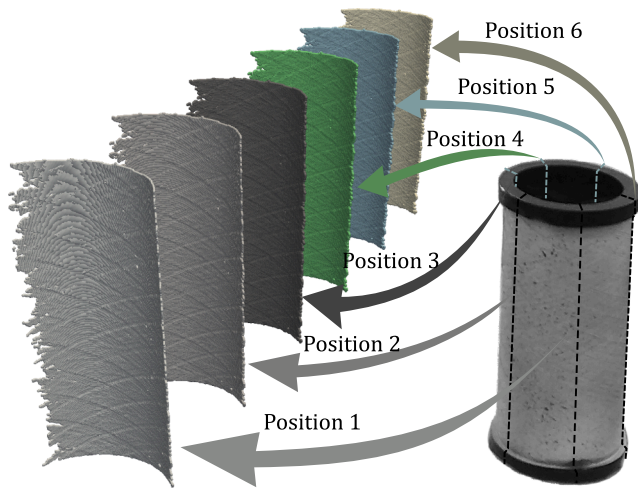
Fig. 10. DIC raw data extracted at each circumferential position. All this data is obtained on the same coordinate system shown in Fig. 9. All adjacent positions are 60° apart.
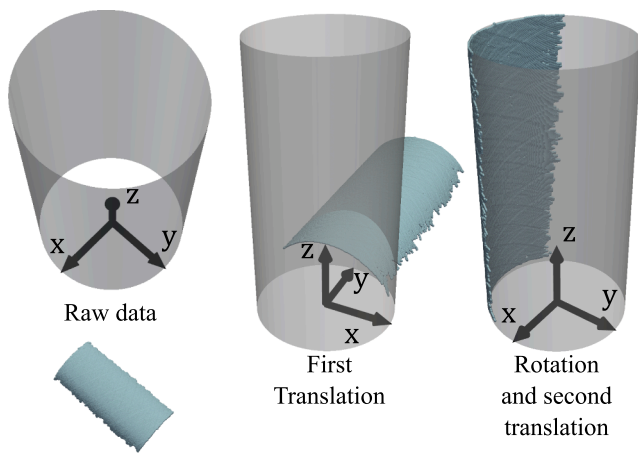

Fig. 11. Best–fit cylinder. Each set of raw data measured at different positions is transformed to a reference cylinder defined using the DIC coordinate system of Fig. 9.

(a) Position 1: 0° (b) Position 2: -60° (c) Position 3: -120°

(d) Position 4: -180° (e) Position 5: -240° (f) Position 6: -300°

Fig. 12. Initial rotation of each DIC transformed data to their nominal position.

(a) Wrong stitching (b) Correct stitching
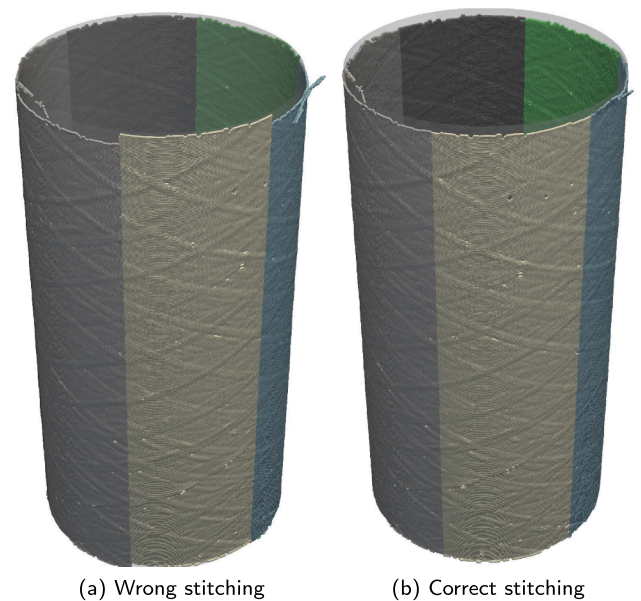
Fig. 13. Comparison between a wrong and a correct stitching. The wrong stitching is simply achieved by rotating and trimming. The correct stitching requires rotating, adjusting according to the optimization given in Eq. (10), and finally trimming.

manufacturing method to produce composite cylinders. Moreover, after the very first report in the literature on variable–angle filament–wound (VAFW) cylinders carried out by Wang et al. [21], on reliability–based design and optimization, it becomes evident that real geometric imperfections and their effects on the mechanical performance of filament–wound shells is yet unknown and unexplored. Almeida Jr. et al. [29] demonstrated the superior tailoring potential and mechanical properties of VAFW cylinders.

Therefore, this work aims at overcoming all these issues by proposing an original and less costly methodology to measure geometric imperfections of VAFW composite cylinders through DIC using only a pair of stereo cameras, still being able to cover the whole circumference of the structure. The methodology on how to stitch each individual measurement to reconstruct the full shell imperfection is described. First, a new best–fit algorithm is developed to accurately determine the outer surface of the cylinder for each measurement. Thus, each measurement is rotated and the adjacent imperfection data compared to determine the exact rotation angle that perfectly stitches each measurement. After trimming each rotated measurement, the complete shell imperfection is achieved.
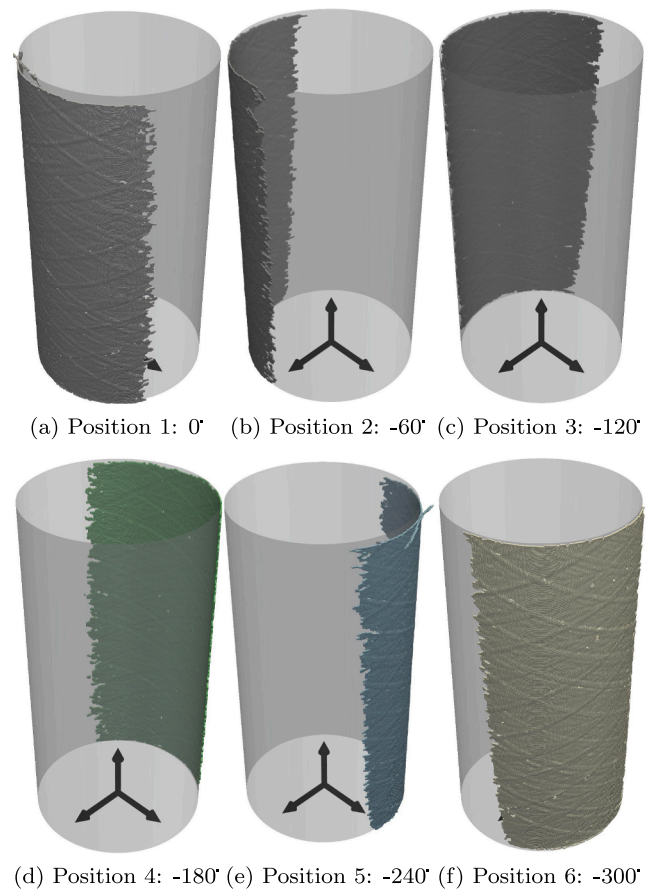
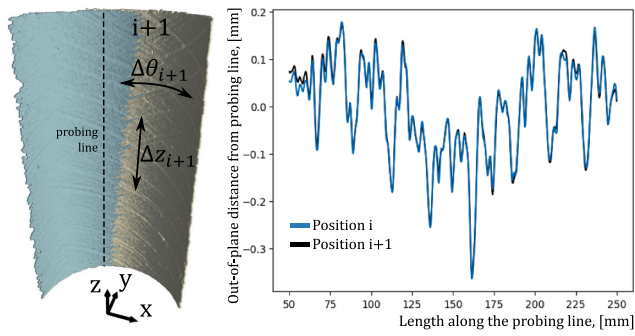**Fig. 14.** Variables $\Delta\theta_{i+1}$ and Δz_{i+1} used to adjust position $i+1$ in order to minimize the difference of out-of-plane distance between positions i and $i+1$, measured from the probing line.

(a) 1 position   (b) 2 positions   (c) 3 positions

(d) 4 positions   (e) 5 positions   (f) 6 positions
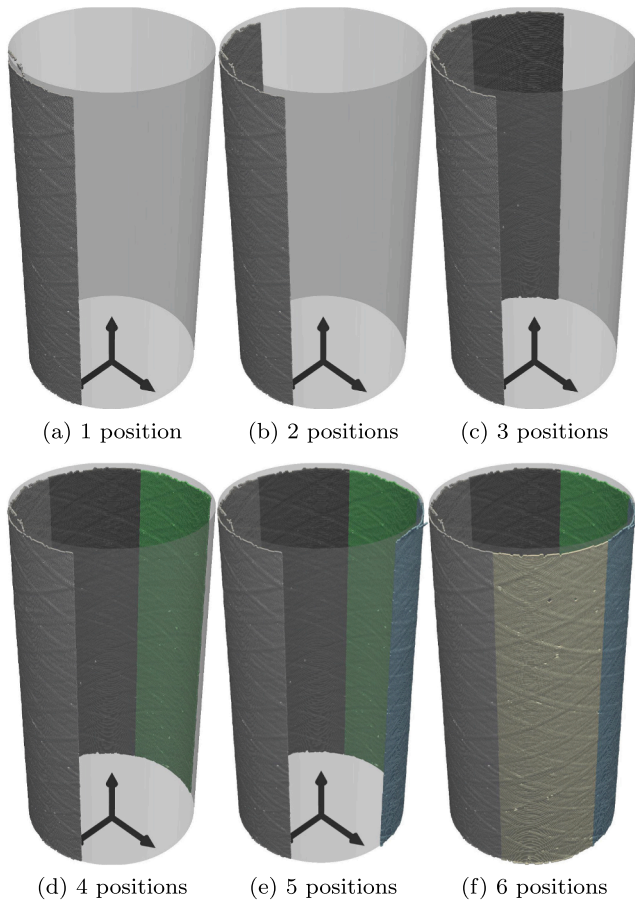
Fig. 15. Stitching steps of each DIC measurement towards the final three-dimensional geometric imperfection.

2. Digital Image Correlation (DIC) system

Digital Image Correlation (DIC) is an optical method mostly used to measure deformations on a surface of a 3D object. The method tracks the gray value pattern in small neighborhoods, called subsets, during deformation. This technique has been proven to be accurate when compared to FE predictions. The commercially available VIC-2D and VIC-3D systems from isi-sys Optical Measurement Solutions GmbH [30] are used in this study. In the present study, the images are captured by a pair of 9 mega-pixel cameras with 50 mm lenses.

Fig. 16. Inner surface of filament-wound cylinder VAFW4-3. The smooth mandrel produces a significantly smoother inner surface on the cylinder compared to the outer surface.
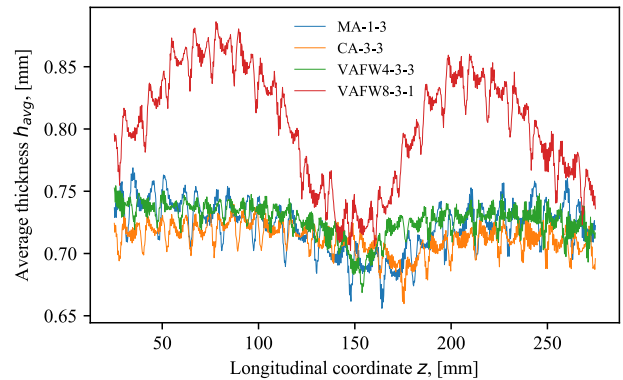
Fig. 17. Average thickness distributions $h_{avg}(z)$ for different VAFW designs.

3. Imperfection measurements

3.1. Cylinders and speckle patterns

Four types of filament-wound cylinder configurations are considered in this study, all having an angle–ply $\pm\theta$ layer that can vary along the axial direction. The four designs optimized in a previous study [29] are: i) **MA** representing the minimum winding angle, with a constant winding angle of $\pm50°$; ii) **CA** with a constant angle of $\pm58°$; iii) **VAFW4** where the cylinder is divided into four frames over the length, and each frame has an angle of $\pm59°$; and iv) **VAFW8** with eight frames and it the following winding angle sequence: <55—57—61—57—57—61—57—55>. All cylinders are symmetric with respect to their mid–length, have a length
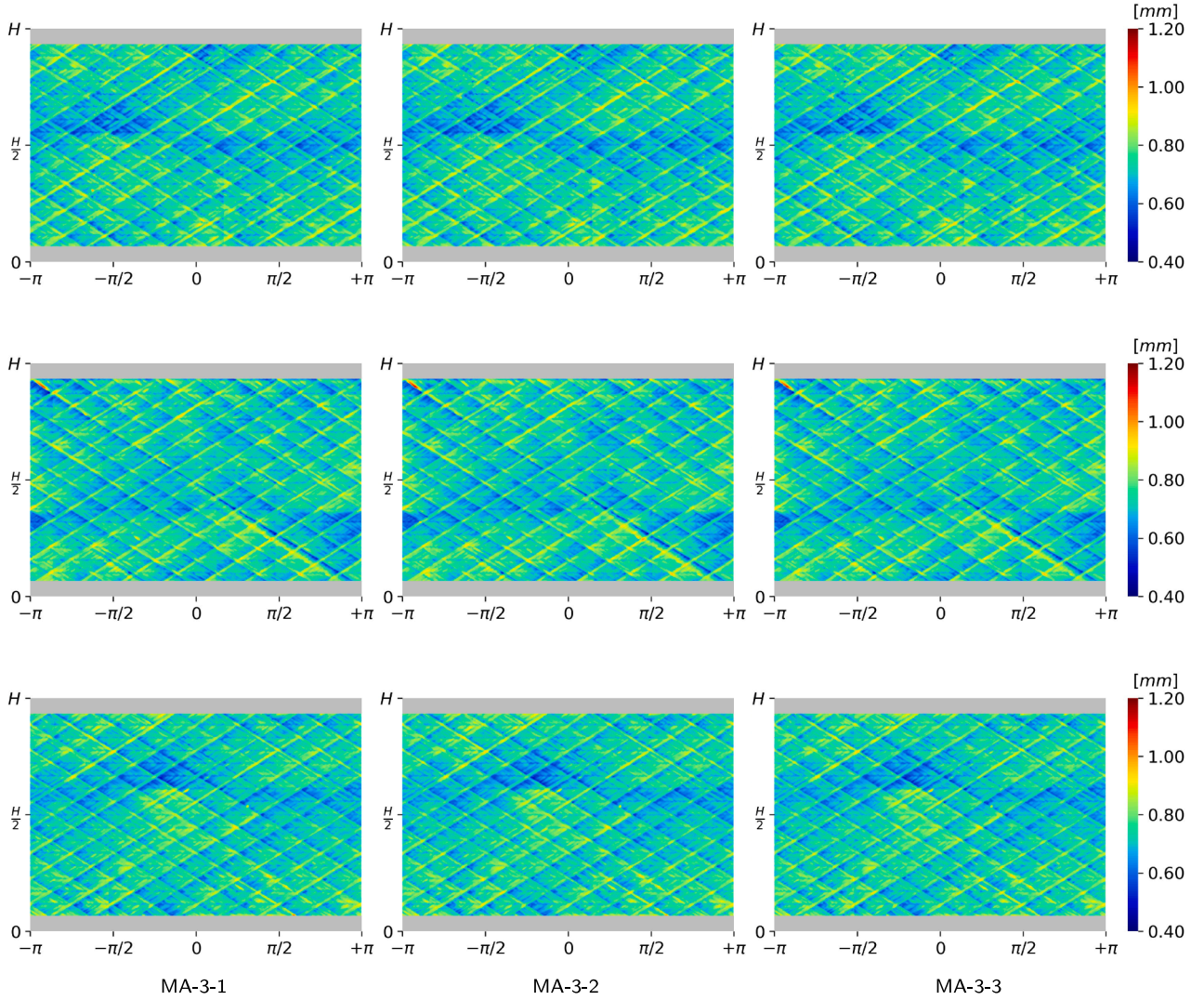
Fig. 18. Stitched thickness imperfection for MA-*i-j*: i^{th} sample, j^{th} measurement using the proposed DIC scheme.

$L = 300$ mm and a homogeneous inner radius $r_{cyl} = 68$ mm.

The material is a carbon/epoxy Toray T700-12 K-50C from TCR Composites. The FW system consists of a KUKA robot model KR 140 L100 with MFTech control and peripheral devices and it has seven degrees of freedom (six axes plus the mandrel rotation). The cylinders are designed in CADWIND FW software [31]. The mandrel plus composite laminate system is cured in an oven with air circulation at 105 °C for 24 h. The system is cooled down to room temperature, and the cylinder is extracted from the mandrel.

The four types of cylinders are shown in Fig. 2, and three cylinders are produced for each family. The cylinders are cast into a metal–filler toughened epoxy resin to improve the load distribution during the compression tests (Fig. 1). After casting, all cylinders are painted with a white layer followed by a speckled pattern. In all cases, the speckle painting is performed by positioning the black painting spray at about 0.5 m away from the cylinders, pointing it slightly tangentially to the cylinder and gently pressing the spray nozzle. The exhaustion air carried the painting mist towards the cylinder. Nonetheless, there is a considerable difference between the speckled patterns for different samples, as shows Fig. 3. For instance, cylinder VAFW4-1 and MA-2 have almost no speckles, whereas MA-1, CA-3, VAFW4-2, VAFW4-3, VAFW8-1 and VAFW8-2 have rather dense speckled patterns. All other samples have patterns within this qualitative range. The size of the speckles is kept small to minimize the loss of imperfection data due to large black-dotted regions.

3.2. DIC setup

The DIC cameras are positioned at about 700 mm from the cylinder, and their height is approximately at the cylinder's mid-plane. A sturdy table is used to support the cylinders during measurements. The computer is placed in a convenient way to look at the monitor while adjusting light and focus, as shown in Fig. 4. The position of the cylinder is marked on the table with a pen; this allows to rotate the samples without changing their original position for which the cameras are calibrated.

3.3. Lighting and focus adjustments

With the cylinder in place, the following steps are taken to adjust the final camera position, camera exposure, artificial light and focus.

1) Initial adjustments in artificial light and camera exposure time. The cameras are positioned according to their aperture size and available space in the lab, as discussed before. With the capture system on, the initial brightness is verified by adjusting the LED panel intensity and position. In the present experimental setup, the ambient light is enhanced with the LED panel. The camera exposure time ranges from 20 to 150 ms, depending on the varying ambient light conditions that is described in the following paragraph.

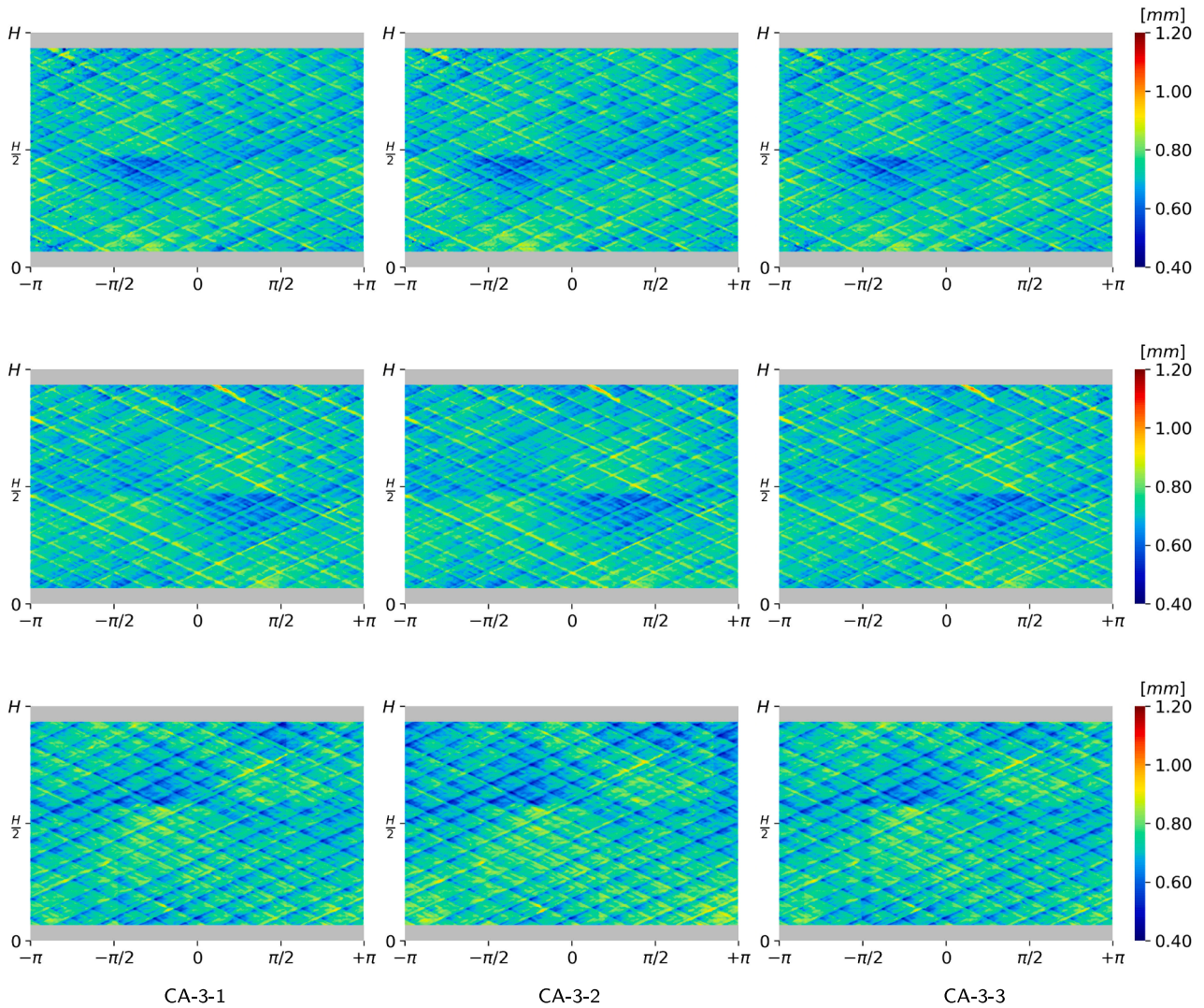**2) Positioning the cameras**. With sufficient brightness, the final

Fig. 19. Stitched thickness imperfection for CA-i-j: ith sample, jth measurement using the proposed DIC scheme.

positioning of the cameras takes place. The cameras are moved laterally and rotated along two axes to make the cylinders appear in the middle of the image, and with both sides aligned with the vertical edges of the photographs. The position is secured by screwing the adjustment bolts tightly.

3) Focus adjustment. The focus adjustment for a cylindrical surface requires finding a compromise between surface depth-coverage and accuracy. Therefore, the optimal focus is not adjusted to be at the outer-most face, but slightly deeper to increase the accuracy on surface points that are more distant from the cameras (Fig. 6). Even with this compromise, the surface topography is less accurate for points that are further from the camera, where the predicted pixel noise can increase up to 5%.

4) Final brightness adjustment. Ideally, one should use a camera exposure time as short as possible, with sufficient diffuse, ambient, light to provide sufficient brightness. Lighting devices, however, usually generate a focused light that can cause undesirable reflections on a cylindrical shell. Therefore, finding the perfect lighting conditions can be somewhat challenging, especially if the ambient light conditions vary during the experiments. For instance, in the Delft Aerospace Structures and Materials Laboratory (DASML), the sunlight switches from one side in the morning to the other side in the afternoon. Moreover, the light conditions change quickly during the experiments because sunlight is

often blocked by passing clouds, as illustrated in Fig. 5. Future solutions for a better measurement setup could make use of a tent to minimize the effect of ambient light and additional LED panels to guarantee sufficient artificial light to outshine the ambient one. This would also have the benefit of allowing minimal exposure times, making the measurements less susceptible to disturbances. The LED panel illustrated in Fig. 4 is used to compensate these fast changing light conditions, such that the methodology proposed here can be employed in nearly any environment with varying natural light conditions. It is worth mentioning that in the worst case one picture took 15 min to be taken until sufficiently good brightness conditions are achieved. Fig. 7 compares the various brightness conditions as presented by the VIC SNAP 3D software [30].

3.4. Calibrating the DIC system

A calibration is performed before each measurement. Three measurements are carried out per cylinder shown in Fig. 2, resulting in a total of 36 measurements. The calibration is highly affected by the focus adjustments explained earlier, such that before each calibration the focus must be checked and adjusted whenever necessary. The marked position of the cylinder on the table guarantees that the cylindrical shell remains in the region for which the focus was calibrated, which is crucial since the measurement process requires rotating the cylinder in
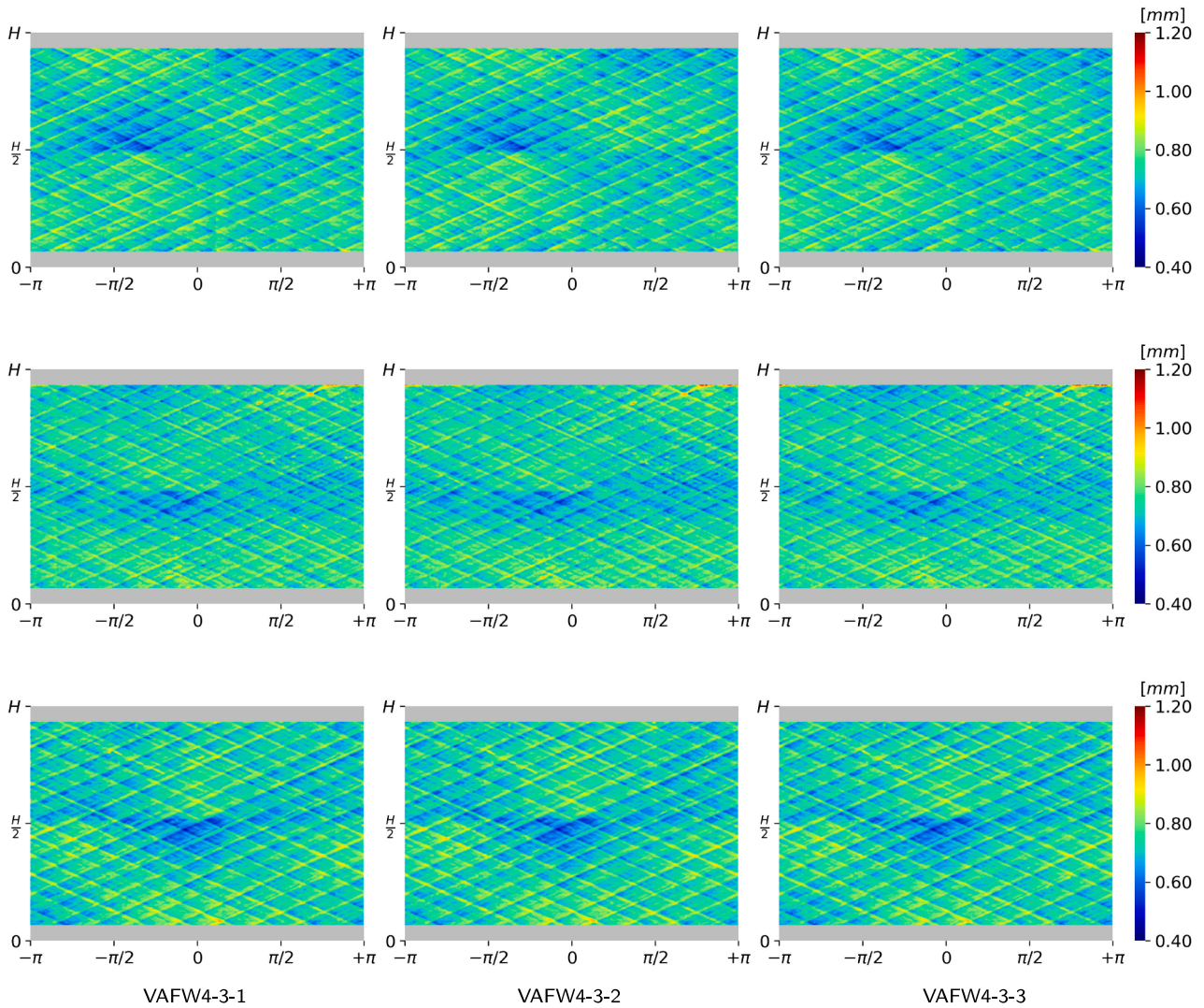
Fig. 20. Stitched thickness imperfection for VAFW4-i-j: ith sample, jth measurement using the proposed DIC scheme.

increments of 60°. As illustrated in Fig. 8, a calibration pattern of 5 mm is used and placed at nine positions that define the extremities of the region of interest being measured. The calibration pattern is always rotated to follow the cylindrical surface to improve the accuracy of the furthest measured points. The pixel error produced by the calibration procedure can be calculated, and among all measurements herein reported this error ranges from 0.014 pixels to 0.049 pixels. Along the 300 mm length of the cylinder there are approximately 3300 pixels, corresponding to 11 pixels/mm; hence, the expected measurement error ranges from 0.001 mm to 0.004 mm. This is the expected error in the regions covered by the calibration pattern. Surface points laying beyond the calibrated area show larger errors and are ignored in the stitching procedure discussed next.

3.5. DIC raw data

The DIC raw data collected in this study is publicly available in [32] and consists of a cloud of points x_i, y_i, z_i for $i = 1, 2, ..., n_{points}$ representing the topography of the measured cylinders at each circumferential position. All points are expressed in terms of the DIC coordinate system *XYZ*, as depicted in Fig. 9.

The position of the cylinders is marked on the measurement table by drawing the contour of the sample with a marker pen, as mentioned

earlier. An arbitrary reference for the circumferential position that corresponds to the 0° angle is defined on the table. Meanwhile, all cylinders are marked at the resin potting region at every 60°, such that a total of 6 circumferential position markers are created. The DIC system is calibrated once when the cylinder is at the circumferential position 0°. When the cylinder is rotated, brightness and focus conditions are always verified, as explained earlier. One DIC picture is taken from each circumferential position, as shown in Fig. 10. The next step consists of stitching the six images into a closed topographic measurement of the entire cylinder. Note, as an example, that Degenhardt et al. [23] used a high-speed DIC setup consisting of 4 pairs of synchronized cameras for a complete coverage of the cylinder circumference, collecting up to 1000 images per second. A similar system could have been used to measured the mid-surface imperfection, but such hardware setup is considerably more costly than the one proposed here.

4. Best-fitting the DIC raw data

For each stereo picture, a partial topography of the cylinder is obtained as a cloud of points. A very large number of points is present since the cameras used have a resolution of 9 mega–pixels. To reduce the amount of data, 1 out of every 4 points was used in both horizontal and vertical directions. Even with this data reduction, the resolution is
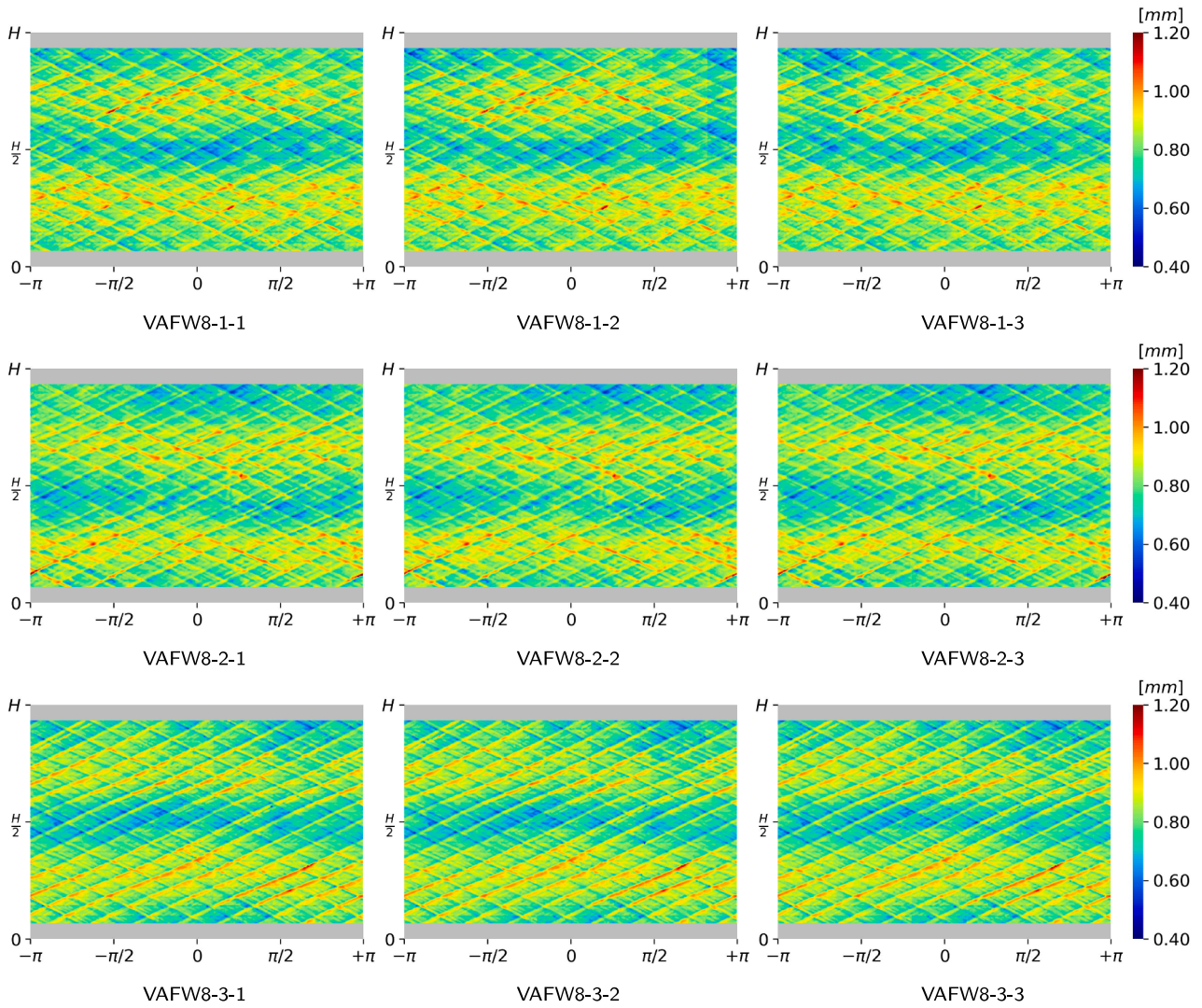
Fig. 21. Stitched thickness imperfection for VAFW8-i-j: ith sample, jth measurement using the proposed DIC scheme.

Table 1
Masses in [g] of each cylinder calculated from the reconstructed imperfection data. The values m_{real} represent the real masses of each cylinder measured after manufacturing.

Cylinder	m_{real}	m_1	m_2	m_3	$m_{avg} \pm \sigma_{m_{avg}}$
MA-1	148	148.05	148.06	148.08	148.06 ± 0.01
MA-2		148.13	148.18	148.14	148.15 ± 0.02
MA-3		148.03	148.07	148.05	148.05 ± 0.02
CA-1	146	146.04	146.07	146.06	146.06 ± 0.01
CA-2		145.97	145.98	145.97	145.97 ± 0.01
CA-3		145.97	145.97	145.97	145.97 ± 0.00
VAFW4-1	149	149.01	149.02	149.03	149.02 ± 0.01
VAFW4-2		149.12	149.16	149.10	149.13 ± 0.03
VAFW4-3		149.07	149.08	149.02	149.06 ± 0.03
VAFW8-1	165	164.77	164.77	164.77	164.77 ± 0.00
VAFW8-2		164.67	164.66	164.65	164.66 ± 0.01
VAFW8-3		164.71	164.71	164.69	164.70 ± 0.01

orders of magnitude smaller than a typical finite element mesh used to predict the collapse of imperfect cylindrical shells [18,33].

With the aim to facilitate the subsequent stitching procedure, and to create a standard format for all geometric imperfections, all DIC raw data points are transformed to a common cylindrical coordinate system (Fig. 11). The data points x_i, y_i, z_i are transformed to new coordinates x_c,

y_c, z_c according to:

$$\begin{Bmatrix} x_c \\ y_c \\ z_c \end{Bmatrix} = [R_z][R_y][R_x] \begin{Bmatrix} x_i + x_0 \\ y_i + y_0 \\ z_i + z_0 \end{Bmatrix} + \begin{Bmatrix} 0 \\ 0 \\ z_1 \end{Bmatrix} \tag{1}$$

where x_0, y_0, z_0 represent translation offsets before rotation, $[R_z][R_y][R_x]$ are rotation matrices, and z_1 is a second translation offset applied after rotation. This two-step translation strategy is not strictly necessary, but it enabled a significantly faster convergence of the surface fitting algorithm. The rotation matrices $[R_z][R_y][R_x]$ are given by:

$$[R_x] = \begin{bmatrix} 1 & 0 & 0 \\ 0 & \cos\alpha & -\sin\alpha \\ 0 & \sin\alpha & \cos\alpha \end{bmatrix} \tag{2}$$

$$[R_y] = \begin{bmatrix} \cos\beta & 0 & \sin\beta \\ 0 & 1 & 0 \\ -\sin\beta & 0 & \cos\beta \end{bmatrix} \tag{3}$$

$$[R_z] = \begin{bmatrix} cos\gamma & -sin\gamma & 0 \\ sin\gamma & cos\gamma & 0 \\ 0 & 0 & 1 \end{bmatrix} \tag{4}$$

where α, β, γ are transformation angles around the x, y, z axes, respectively, and measured according to the right-hand rule, see Fig. 11.

A total of seven parameters ($\alpha, \beta, \gamma, x_0, y_0, z_0, z_1$) are needed in Eq. (1) to transform the DIC raw data points x_i, y_i, z_i to the desired coordinate system x_c, y_c, z_c. When fitting a perfect cylinder, γ is not needed and can be set to $\gamma = 0$. The other six parameters are obtained from a first best-fitting optimization governed by:

$$
\begin{aligned}
\text{minimize} \quad & \sum_{c=1}^{n_{points}} \sqrt{x_c^2 + y_c^2} - r_{cyl} \\
\text{with respect to} \quad & r_{cyl}, \alpha, \beta, x_0, y_0, z_0 \\
\text{subject to} \quad & r_{min} \leqslant r_{cyl} \leqslant r_{max} \\
& -\pi \leqslant \alpha, \beta, \gamma \leqslant +\pi \\
& -\infty \leqslant x_0, y_0, z_0 \leqslant +\infty
\end{aligned}
\tag{5}
$$

where r_{cyl} can vary between r_{min} and r_{max} or be set to a constant value, and in the present study it is fixed at $r_{cyl} = 68$ mm, which is the radius of the mandrel used to manufacture the cylinders. Similarly to Wang et al. [34], the optimization of Eq. (5) is solved using a nonlinear least-squares method, which in the case of the present study is the `scipy.optimize.least_squares` function available in SciPy [35].Because the focus is not uniform throughout the cylindrical surface, points outside the focus plane have a relatively larger error than those in focus. These variations can be corrected using the best-fit elliptic cylinder equation, detailed in Appendix A. For the best-fit elliptic cylinder, the transformation angle γ must be included as a design variable in the optimization procedure. Therefore, after the best-fit cylinder optimization (Eq. (5) with a constant value of r_{cyl}), a second optimization is conducted to determine γ, a, b according to:

$$
\begin{aligned}
\text{minimize} \quad & \sum_{c=1}^{n_{points}} \sqrt{x_c^2 + y_c^2} - r(\theta) \\
\text{with respect to} \quad & \gamma, a, b \\
\text{subject to} \quad & -\pi \leqslant \gamma \leqslant +\pi \\
& 0.9 r_{cyl} \leqslant a, b \leqslant 1.1 r_{cyl}
\end{aligned}
\tag{6}
$$

where $\theta = \arctan y_c / x_c$; the elliptical radius $r(\theta)$ is calculated with Eq. (14); a, b are respectively the major and the minor radii of a best-fit elliptic cylinder, to be determined by the nonlinear least-squares optimizer. The next best-fit step consists of calculating the axial translation z_1 that is used in Eq. (1). This is done based on:

$$
\begin{aligned}
\text{minimize} \quad & \sum_{c=1}^{n_{points}} \Delta z_c \\
\text{with respect to} \quad & z_1 \\
\text{subject to} \quad & -\infty \leqslant z_1 \leqslant +\infty
\end{aligned}
\tag{7}
$$

with Δz_c calculated using Eq. (8) that represents the sum of distances of all points laying outside the inner cylindrical shell domain delimited using the cylinder height H, and on the length of the resin potting l_p illustrated in Fig. 1.

$$
\Delta z_c = \begin{cases} \Delta z_c = z_c - (H - l_p) & z_c > (H - l_p) \\ \Delta z_c = 0 & l_p < z_c < (H - l_p) \\ \Delta z_c = l_p - z_c & z_c < l_p \end{cases}
\tag{8}
$$

Note that the DIC raw data may contain points located in the resin potting areas or even on the table, and these can have a negative effect on the best-fit optimization. To avoid this, the DIC raw data points are clipped before the optimization with the following clipping box:

$$
\begin{aligned}
x_{min}, x_{max} &= -\infty, +\infty \\
y_{min}, y_{max} &= -130 \; mm, +120 \; mm \\
z_{min}, z_{max} &
\end{aligned}
\tag{9}
$$

where $z_{max} = (z_{imax} + 1)[mm]$ and $z_{min} = (z_{max} - R(1 - \cos 45°) - 1)[mm]$. The value z_{imax} is determined for each DIC raw data corresponding to one circumferential position, as shown in Fig. 9. The limits y_{min}, y_{max} are chosen to remove spurious points from the resin potting areas. Despite the points outside the clipping box are ignored during the best-fit optimization steps, they also undergo the transformation given by Eq. (1) and are kept for the stitching operation, which is described next.

5. Stitching methodology

After best-fitting the DIC raw data points to the desired coordinate system presented in Fig. 11, each measurement is rotated to its nominal circumferential position, as shown in Fig. 12. Simply trimming the data of each angular position and then assembling each section would create a topographic pattern with significant discontinuities, as illustrated in Fig. 13a. To correct this issue, an automated stitching scheme is proposed to create smooth three-dimensional imperfection patterns, as shown in Fig. 13b. Each pair of adjacent DIC measurements, named positions i and $i + 1$, are stitched separately. A probing line is defined at the circumferential position that corresponds to the frontier between positions i and $i + 1$. For instance, between positions 1 and 2 the probing line is located at $-30°$; between 2 and 3 at $-90°$ and so forth. The probing line is located at a coordinate that corresponds to the mid-surface, here assumed to be at the mean value of all $r_c = \sqrt{x_c^2 + y_c^2}$, with r_c representing the radial coordinates of all points among positions i and $i + 1$. During the stitching process, the points belonging to position $i + 1$ are adjusted circumferentially by a value $\Delta\theta_{i+1}$ and longitudinally by a value Δz_{i+1}, according to:

$$
\begin{aligned}
\text{minimize} \quad & \sum_{c=1}^{n_p} (\Delta r_{ci} - \Delta r_{ci+1})^2 \\
\text{with respect to} \quad & \Delta\theta_{i+1}, \Delta z_{i+1} \\
\text{subject to} \quad & -10° \leqslant \Delta\theta_{i+1} \leqslant +10° \\
& -10 \; mm \leqslant \Delta z_{i+1} \leqslant +10 \; mm
\end{aligned}
\tag{10}
$$

where n_p is the number of points along the probing line,here fixed at $n_p = 1000$; $\Delta r_{ci}, \Delta r_{ci+1}$ are the out-of-plane distances between the probing line and the positions i and $i + 1$,respectively. Fig.14 illustrates the stitching variables $\Delta\theta_{i+1}, \Delta z_{i+1}$,and includes a plot of Δr_{ci} and Δr_{ci+1} as a function of position along the probing line. For each cylinder,the optimization in Eq.(10) is run six times.First,position 1 is taken as a reference (Fig.15a) and the first stitching optimization finds $\Delta\theta_2, \Delta z_2$ (Fig.15b).This is repeated for each probing line until the final stitching step finds the adjustment required for position 1, $\Delta\theta_1$ and Δz_1. In the

end,all $\Delta\theta_i$ and Δz_i for $i = 2,3,4,5,6$,can be offset such that $\Delta\theta_1 = 0$ and $\Delta z_1 = 0$.The initial guess for $\Delta\theta_i, \Delta z_i$ in the optimization of Eq.(10) can have a significant influence on the result.Therefore, the optimization for each $\Delta\theta_i, \Delta z_i$ is based on a total of 121 equally spaced initial points, covering circumferential offset values ranging from $-10°$ to $+10°$,and axial offset values ranging from -20 mm to $+20$ mm. The best initial guess is determined by finding the initial point$\Delta\theta_i, \Delta z_i$ that results in the minimum value of $\sum_{i=1}^{n_p}(\Delta r_i - \Delta r_{i+1})^2$, which is the same function being minimized in the optimization described in Eq. (10).

6. Stitching results

The steel-based mandrel used to manufacture the filament–wound cylinders has a smooth surface, resulting in a very low imperfection signature at the inner surface. Fig. 16 shows the inner surface of cylinder CA-2, where the different tow orientations can be seen. Assuming a smooth inner surface, the three-dimensional stitched outer-surface topology can be used to calculate the thickness imperfection patterns generated by the FW manufacturing process. Figs. 18–21 show the stitched imperfections for the four families of cylinders considered in this study (see Fig. 2). In each figure, the results are shown for three different cylinders (rows) and each measurement was repeated three times (columns) to evaluate the variability of the proposed technique. The differences between each column are negligible, which demonstrates that the proposed technique offers a high repeatability. For each family of cylinder, there are noticeable differences between the three samples (rows), indicating that the technique has the accuracy needed to detect small differences in the imperfection patterns. In addition, these results are available in a public dataset [36].

The thickness averaged over the circumference $h_{avg}(z)$ is plotted in Fig. 17 as a function of the axial coordinate z for one cylinder in each family. Results are given for $25\ mm \leqslant z \leqslant 275\ mm$ only to exclude the regions close to the resin potting. One approach to verify these thickness profiles is to use them to calculate the mass of the cylinder and compare this result to their actual mass. The mass of each cylinder can be calculated by:

$$m_{cyl} = \int_{z=0\ mm}^{300\ mm}\int_{\theta=0}2\pi\int_{r=r_{cyl}}^{r_{cyl}+h(r,\theta)}\rho r dr d\theta dz \qquad (11)$$

where $h(r,\theta)$ is the local thickness measurement; $\rho = 1600$ kg/m^3 is the density of the material; and $r_{cyl} = 68$ mm is the mandrel radius. Assuming an average thickness $h_{avg}(z)$, this equation can be approximated as:

$$m_{cyl} \approx 2\pi r_{cyl}\rho\frac{300}{250}\int_{z=25\ mm}^{z=275\ mm}h_{avg}(z)dz \qquad (12)$$

where the ratio 300/250 must be used to compensate the missing region close to the edges. Table 1 presents the calculated mass for all reconstructed geometric imperfections. The columns m_1, m_2, m_3 represent the three DIC measurements for each sample. The standard deviation of the calculated mass is extremely small, with a maximum of ± 0.03 g. The real mass of each sample, measured after manufacturing, is also included in

Table 1. In all cases, there is an excellent agreement between the calculated and real mass, which is evidence that the methodology proposed here offers a high level of accuracy to measure geometric imperfection profiles. The geometric imperfections herein presented are used in the nonlinear finite element analyses of Almeida Jr. et al. [29].

7. Conclusions

A novel methodology was presented to measure the geometric imperfection pattern of composite cylinders using digital image correlation (DIC). The experimental setup is simple and requires only a pair of cameras. DIC is largely applied as a technique to measure displacement and strain fields, and the present study is the first one to extend its applicability towards measuring geometric imperfections. The method proposed here covers all steps of the process from image acquisition to the post-processing and stitching needed to reconstruct three-dimensional imperfection patterns from DIC raw data.The proposed methodology is applicable to any shell of revolution and assumes that the inner mold surface is smooth, such as in the case of filament-wound structures, and a large class of shells manufactured by means of a smooth inner mold.Future studies should focus on uncertainty quantification and reliability-based analyses to assess the sensitivity of the stability behavior of variable-angle filament-wound (VAFW) cylinders to the error of the herein proposed imperfection measurement technique, and preferably cross-checking with other imperfection measurement techniques, for small and large structures.

CRediT authorship contribution statement

Saullo G.P. Castro: Conceptualization, Methodology, Software, Formal analysis, Investigation, Validation, Data curation, Supervision, Resources, Writing - original draft. **José Humberto S. Almeida Jr.:** Formal analysis, Investigation, Funding acquisition, Validation, Writing - original draft, Writing - review & editing. **Luc St-Pierre:** Writing - review & editing, Resources. **Zhihua Wang:** Investigation, Methodology.

Declaration of Competing Interest

The authors declare that they have no known competing financial interests or personal relationships that could have appeared to influence the work reported in this paper.

Appendix A. Elliptic cylinder

The stitching procedure can be improved by fitting the data points to an elliptic cylinder instead of a circular one. Using the coordinate system in Fig. 11, the perfect elliptic perimeter can be represented in Cartesian coordinates as:

$$\frac{x^2}{a^2} + \frac{y^2}{b^2} = 1 \qquad (13)$$

where x, y are points laying perfectly on the ellipse's surface, a is the major and b the minor radii of the ellipse. Substituting x and y with the polar relations:

$$x = r(\theta)\cos\theta \qquad y = r(\theta)\sin\theta$$

into Eq. (13) gives the perfect ellipse's radius $r(\theta)$:

$$r(\theta) = \frac{ab}{\sqrt{(a\sin\theta)^2 + (b\cos\theta)^2}} \tag{14}$$

First, all measured DIC points are transformed to x_c, y_c, z_c coordinates according to Eq. (1). Second, the measured radius of each point, r_c, and its corresponding circumferential position θ_c, can be calculated as:

$$\theta_c = \tan^{-1}(y_c/x_c)$$
$$r_c = \sqrt{x_c^2 + y_c^2} \tag{15}$$

The measured radius r_c differs from the perfect elliptic cylinder radius (for a specific circumferential position θ_c). This difference represents a geometric imperfection for this data point, and it is here represented by Δr_c:

$$\Delta r_c = r_c - r(\theta_c) \tag{16}$$

This imperfection value can be remapped to a best-fit cylinder, as the one illustrated in Fig. 11, by adding the geometric imperfection to the best-fit radius, such that a new radial position r_{cnew} is calculated:

$$r_{cnew} = R + \Delta r_c \tag{17}$$

Finally, the new Cartesian coordinates for each data point can be retrieved using:

$$x_{cnew} = r_{cnew}\cos\theta_c$$
$$y_{cnew} = r_{cnew}\sin\theta_c$$
$$z_{cnew} = z_c \tag{18}$$

Appendix B. Data Availability Statement

The raw data [32] and final three-dimensional imperfections [36] obtained in the present work are already publicly available. The scripts used to best-fit and stitch the DIC data can be made available under request per email to the corresponding authors.

References

[1] Arbocz J, Hilburger MW. Toward a probabilistic preliminary design criterion for buckling critical composite shells. AIAA J 2005;43(8):1823–7. https://doi.org/10.2514/1.11368.

[2] Hilburger MW, Nemeth MP, Starnes JH. Shell buckling design criteria based on manufacturing imperfection signatures. AIAA J 2006;44(3):654–63. https://doi.org/10.2514/1.5429.

[3] Croll JG. Towards a rationally based elastic-plastic shell buckling design methodology. Thin-Walled Struct 1995;23(1–4):67–84. https://doi.org/10.1016/0263-8231(95)00005-X.

[4] Southwell RV. On the general theory of elastic stability. Philos Trans R Soc London. Ser A 1914;213(497–508):187–244. https://doi.org/10.1098/rsta.1914.0005.

[5] Flügge W. Die Stabilität der Kreiszylinderschale. Ingenieur-Archiv 1932;3(5):463–506. https://doi.org/10.1007/BF02079822.

[6] Donnell LH. A new theory for the buckling of thin cylinders under axial compression and bending. ASME Trans 1934;56:795–806.

[7] Von Kármán T, Tsien H-S. The buckling of thin cylindrical shells under axial compression. J Aeronaut Sci 1941;8(8):303–12. https://doi.org/10.2514/8.10722.

[8] Koiter WT. On the stability of elastic equilibrium, Ph.D. thesis, Polytechnic Institute of Delft, Delft, the Netherlands; 1945.

[9] Peterson J, Seide P, Weingarten V. Buckling of thin-walled circular cylinders – NASA SP-8007, Tech. rep. Virginia, USA: NASA; 1968. https://ntrs.nasa.gov/citations/19690013955.

[10] Sheinman I, Simitses GJ. Buckling and postbuckling of imperfect cylindrical shells under axial compression. Comput Struct 1983;17(2):277–85. https://doi.org/10.1016/0045-7949(83)90016-0.

[11] Simitses GJ, Shaw D, Sheinman I. Imperfection sensitivity of laminated cylindrical shells in torsion and axial compression. Compos Struct 1985;4(4):335–60. https://doi.org/10.1016/0263-8223(85)90032-7.

[12] Wilkins DJ, Love TS. Combined compression-torsion buckling tests of lamianted composite cylindrical shells. In: AIAA/ASME/SAE 15th structures, structural dynamics and materials conference, AIAA, ASME, SAE, Las Vegas, Nevada, USA; 1974. p. 1–8. doi:10.1016/0263-8223(85)90032-7.

[13] Chryssanthopoulos MK, Giavotto V, Poggi C. Characterization of manufacturing effects for buckling-sensitive composite cylinders. Compos Manuf 1995;6(2):93–101. https://doi.org/10.1016/0956-7143(95)99649-D.

[14] Arbocz J, Babcock CD. Prediction of buckling loads based on experimentally measured initial imperfections. In: Buckl Struct. Berlin Heidelberg: Springer; 1976. p. 291–311. https://doi.org/10.1007/978-3-642-50992-6_24.

[15] Bisagni C. Numerical analysis and experimental correlation of composite shell buckling and post-buckling. Compos Part B 2000;31(8):655–67. https://doi.org/10.1016/S1359-8368(00)00031-7.

[16] Khot N, Venkayya V. Effect of fiber orientation on initial postbuckling behavior and imperfection sensitivity of composite cylindrical shells. Tech. rep. 1970.

[17] Taheri-Behrooz F, Omidi M, Shokrieh MM. Experimental and numerical investigation of buckling behavior of composite cylinders with cutout. Thin-Walled Struct 2017;116:136–44. https://doi.org/10.1016/j.tws.2017.03.009.

[18] Castro SGP, Zimmermann R, Arbelo MA, Khakimova R, Hilburger MW, Degenhardt R. Geometric imperfections and lower-bound methods used to calculate knock-down factors for axially compressed composite cylindrical shells. Thin-Walled Struct 2014;74:118–32. https://doi.org/10.1016/j.tws.2013.08.011.

[19] Hühne C, Rolfes R, Breitbach E, Teßmer J. Robust design of composite cylindrical shells under axial compression – Simulation and validation. Thin-Walled Struct 2008;46(7–9):947–62. https://doi.org/10.1016/j.tws.2008.01.043.

[20] Castro SGP, Zimmermann R, Arbelo MA, Degenhardt R. Exploring the constancy of the global buckling load after a critical geometric imperfection level in thin-walled cylindrical shells for less conservative knock-down factors. Thin-Walled Struct 2013;72:76–87. https://doi.org/10.1016/j.tws.2013.06.016.

[21] Wang Z, Almeida Jr. JHS, St-Pierre L, Wang Z, Castro SGP. Reliability-based buckling optimization with an accelerated Kriging metamodel for filament-wound variable angle tow composite cylinders. Compos Struct 2020;254:112821. https://doi.org/10.1016/j.compstruct.2020.112821.

[22] Di Pasqua MF, Khakimova R, Castro SGP, Arbelo MA, Riccio A, Raimondo A, et al. Investigation on the geometric imperfections driven local buckling onset in composite conical shells. Appl Compos Mater 2016;23(4):879–97. https://doi.org/10.1007/s10443-016-9490-7.

[23] Degenhardt R, Kling A, Klein H, Hillger W, Goetting HC, Zimmermann R, Rohwer K, Gleiter A. Experiments on buckling and postbuckling of thin-walled CFRP structures using advanced measurement systems. Int J Struct Stab Dyn 2007;07(02):337–58. https://doi.org/10.1142/S0219455407002253.

[24] Khakimova R, Castro SGP, Wilckens D, Rohwer K, Degenhardt R. Buckling of axially compressed CFRP cylinders with and without additional lateral load: Experimental and numerical investigation. Thin-Walled Struct 2017;119:178–89. https://doi.org/10.1016/j.tws.2017.06.002.

[25] Eberlein DJ. Composite cylindrical shell buckling: simulation & experimental correlation, Ph.D. thesis, Delft University of Technology; 2019. http://resolver. tudelft.nl/uuid:cbaf7f4f-ae81-4f54-ab75-c830d8c5cf6e.

[26] Skukis E, Ozolins O, Andersons J, Kalnins K, Arbelo MA. Applicability of the vibration correlation technique for estimation of the buckling load in axial compression of cylindrical isotropic shells with and without circular cutouts. Shock Vibr 2017. https://doi.org/10.1155/2017/2983747.

[27] Labans E, Bisagni C. Buckling and free vibration study of variable and constant-stiffness cylindrical shells. Compos Struct 2019;210:446–57. https://doi.org/10.1016/j.compstruct.2018.11.061.

[28] Azevedo CB, Almeida Jr. JHS, Flores HF, Eggers F, Amico SC. Influence of mosaic pattern on hygrothermally-aged filament wound composite cylinders under axial compression. J Compos Mater 2020;54(19):2651–9. https://doi.org/10.1177/0021998319899144.

[29] Almeida Jr. JHS, St-Pierre L, Ribeiro ML, Volnei Tita R, Amico SC, Castro SGP, et al. Design, modeling, optimization, manufacturing and testing of variable-angle filament-wound cylinders. Composites Part B: Engineering 2021. https://doi.org/10.1016/j.compositesb.2021.109224. In press.

[30] DIC Systems – isi-sys; 2020. http://www.isi-sys.com/category/products/dic-systems/.

[31] Laval C. CADWIND 2006–20 years of filament winding experience. Reinf Plast 2006;50(2):34–7. https://doi.org/10.1016/S0034-3617(06)70913-4.

[32] Castro SGP, Almeida Jr. JHS. VAFW cylinders 2020, S1, S2, S4, S8, DIC raw data. (Version 2021-03-16) [Data set]. 2021. https://doi.org/10.5281/zenodo.4608398.

[33] Castro SGP, Reichardt J, Lozano E. DESICOS Plug-in for Abaqus Feb. 2021. https://doi.org/10.5281/zenodo.4506587.

[34] Wang B, Zhu S, Hao P, Bi X, Du K, Chen B, Ma X, Chao YJ. Buckling of quasi-perfect cylindrical shell under axial compression: A combined experimental and numerical investigation. Int J Solids Struct 2018;130–131:232–47. https://doi.org/10.1016/j.ijsolstr.2017.09.029.

[35] Virtanen P, Gommers R, Oliphant TE, Haberland M, Reddy T, Cournapeau D, Burovski E, Peterson P, Weckesser W, Bright J, van der Walt SJ, Brett M, Wilson J, Millman KJ, Mayorov N, Nelson ARJ, Jones E, Kern R, Larson E, Carey CJ, Polat İ, Feng Y, Moore EW, VanderPlas J, Laxalde D, Perktold J, Cimrman R, Henriksen I, Quintero EA, Harris CR, Archibald AM, Ribeiro AH, Pedregosa F, van Mulbregt P. SciPy 1.0 Contributors, SciPy 1.0: Fundamental Algorithms for Scientific Computing in Python. Nat Methods 2020;17:261–72. https://doi.org/10.1038/s41592-019-0686-2.

[36] Castro SGP, Almeida Jr. JHS. VAFW cylinders 2020, S1, S2, S4, S8, stitched imperfections. (Version 2021-03-04) [Data set]. 2021. https://doi.org/10.5281/zenodo.4581164.